

Reconstructing Pristine Molecular Orbitals from Scanning Tunneling Microscopy Images via Artificial Intelligence Approaches

Yu Zhu^{1†}, Renjie Xue^{2†}, Hao Ren³, Yicheng Chen¹,
Wenjie Yan¹, Bingzheng Wu¹, Sai Duan^{1,4*}, Haiming Zhang^{2*},
Lifeng Chi^{2*}, Xin Xu^{1,4*}

¹Collaborative Innovation Center of Chemistry for Energy Materials, Shanghai Key Laboratory of Molecular Catalysis and Innovative Materials, MOE Key Laboratory of Computational Physical Sciences, Department of Chemistry, Fudan University, Shanghai, 200433, P. R. China.

²Jiangsu Key Laboratory for Carbon-Based Functional Materials and Devices, Institute of Functional Nano and Soft Materials (FUNSOM), Soochow University, Suzhou, 215123, Jiangsu, P. R. China.

³School of Materials Science and Engineering, China University of Petroleum (East China), Qingdao, 266580, Shandong, P. R. China.

⁴Hefei National Laboratory, Hefei, 230088, P. R. China.

*Corresponding author(s). E-mail(s): duansai@fudan.edu.cn;
hmzhang@suda.edu.cn; chilf@suda.edu.cn; xxchem@fudan.edu.cn;

[†]These authors contributed equally to this work.

Abstract

Molecular orbital (MO) is one of the most fundamental concepts for molecules, relating to all branches of chemistry, while scanning tunneling microscopy (STM) has been widely recognized for its potential to measure the spatial distribution of MOs. However, the precise characterization of MO with high resolution in real space is a long-standing challenge owing to the inevitable interference of high-angular-momentum contributions from functionalized tips in STM. Here, leveraging advances in artificial intelligence for image recognition, we establish a physics-driven deep-learning network, named STM-Net, to reconstruct MOs from high-resolution STM images with a functionalized tip, taking advantage of

the separable characteristics of different angular momentum contributions. We demonstrate that STM-Net can be directly applied to a variety of experimental observations, successfully reconstructing pristine MO features for molecules under diverse conditions. Moreover, STM-Net can adapt to various states of the functionalized tip and the substrate, illustrating the broad applicability of our physics-driven framework. These results pave the way for accurate characterization of MO with high resolution, potentially leading to new insights and applications for this fundamental concept in chemistry.

Molecules are systems where nuclei are interconnected through chemical bonds formed by shared electrons. These electrons act as a “glue”, counterbalancing the electrostatic repulsion between positively charged nuclei and giving rise to molecular orbitals (MOs). As a fundamental concept rooted in quantum mechanics[1], MOs represent one of the most pivotal concepts in chemical science. Specifically, frontier MOs, the highest occupied molecular orbital (HOMO) and the lowest unoccupied molecular orbital (LUMO), play a critical role in governing chemical reactivity in both ground and excited states[2, 3]. Understanding the distribution and energy levels of MOs provides a foundation for addressing a wide range of chemical challenges. Despite ongoing debates regarding the direct measurement of MOs[4, 5], significant efforts[6–8] have been devoted to developing experimental and theoretical approaches to probe their characteristics by correlating observable phenomena with MO characteristics[9, 10].

Among these techniques, scanning tunneling microscopy (STM) stands out for its ability to provide high-resolution spatial information on MOs in real space[7–9, 11–13]. By utilizing the energy conservation law during elastic electron tunneling, STM can measure the resonance energies that correspond to the energy levels of MOs. Furthermore, based on the Tersoff-Hamann theory[10], for sufficiently decoupled molecules, constant-height imaging under an *s*-wave tip (typically a metallic tip) can be related to the MO’s spatial distribution, yielding a mapping $I_s(x, y) \propto |\phi(x, y, z_0)|^2$, where I_s refers to the *s*-wave tunneling current, ϕ represents the MO at the resonant energy level, and $\{x, y, z_0\}$ denotes the Cartesian coordinate of the metallic tip apex[10, 11, 14]. However, the inherent diffuse nature of the *s*-wave, controlled by the material’s work function, imposes limitations on the resolution achievable with metallic tips. While these tips produce physically interpretable STM images[10], their limited resolution[14] hinders a detailed, high-resolution imaging of MOs.

Functionalized tips, on the other hand, offer enhanced resolution in STM imaging, allowing for the visualization of MOs with finer features[14]. However, this enhancement comes at a cost, such that high-angular-momentum contributions are inevitably introduced to the tunneling current[14, 15]. For instance, the commonly used CO-decorated tip introduces a *p*-wave contribution, which can be expressed as $I_p(x, y) \propto \left| \frac{\partial \phi(x, y, z_0)}{\partial x} \right|^2 + \left| \frac{\partial \phi(x, y, z_0)}{\partial y} \right|^2$, leading to undesirable details other than MOs in STM images[11, 14, 15]. In most cases, the contributions of I_s (from the *s*-wave) and I_p (from the *p*-wave) to the total tunneling current of CO-decorated tips are comparable[14, 16, 17]. Consequently, while functionalized tips enable high-resolution

imaging, the resultant images cannot be directly interpreted as the MO spatial distribution. This creates a fundamental dilemma between achieving high-resolution features with a functionalized tip and obtaining a direct visualization of MOs with a low-resolution metallic tip.

Essentially, the aforementioned dilemma represents an image transformation issue, i.e., how to disentangle and extract physically meaningful components from a high-resolution image that contains extraneous details. We note the unprecedented success of artificial intelligence (AI) in image processing[18, 19], exemplified by breakthroughs such as AlexNet[20] in the ImageNet challenge, which catalyzed the rapid advancement of deep learning. While AI algorithms have achieved significant progress across various domains[21, 22], their most transformative impact has been in the field of image processing. Currently, advanced algorithms, such as U-Net[23], generative adversarial networks[24], and diffusion models[25], are widely applied to enhance image resolution and quality. In the context of STM, however, the application of AI algorithms has predominantly focused on optimizing experimental workflows[26–28], with limited exploration of its potential for interpreting STM images. A major obstacle to this application is the interdependence of two critical factors, namely, the lack of sufficient high-quality data and the absence of tailored algorithms. In this work, we address this challenge by developing STM-Net, a physics-driven deep learning network that leverages advanced image segmentation algorithms to reconstruct pristine MO distribution from high-resolution STM images obtained using functionalized CO tips. This framework demonstrates exceptional versatility, effectively handling complex molecular structures and diverse experimental conditions.

Results and discussion

Development of STM-Net

We start by comparing the characteristics of *s*- and *p*-wave contributions to select an efficient algorithm (Fig. 1). For the fully symmetric *s*-wave, significant tunneling occurs when the tip is placed over regions of high electron density, while at the MO nodes, the current is substantially reduced due to quantum destructive interference (Fig. 1a). In contrast, *p*-wave tips produce low current in MO regions of high electron density but high current at the nodes owing to the same mechanism of quantum interference (Fig. 1b). It is important to note that images from a sole *s*-wave tip have generally low image resolution[14], while the commonly used CO-decorated tips often exhibit comparable *s*- and *p*-wave contributions[14, 16, 17]. These observations pose challenge for obtaining images of pristine MOs with high-resolution. However, the spatially separable nature of *s*- and *p*-wave signals offers an opportunity to differentiate themselves using AI algorithms.

To this end, we constructed a dataset of STM images for the HOMO and LUMO of 159 representative phenyl-based polycyclic aromatic hydrocarbons (PAHs) from the COMPAS project[29], using both pure metal and CO-functionalized tips (see Methods for details). These molecules were deliberately selected based on their suitability for physisorption and the feasibility in experiments via on-surface synthesis. To avoid the lengthy process of experimental measurements, we utilized a highly-accurate

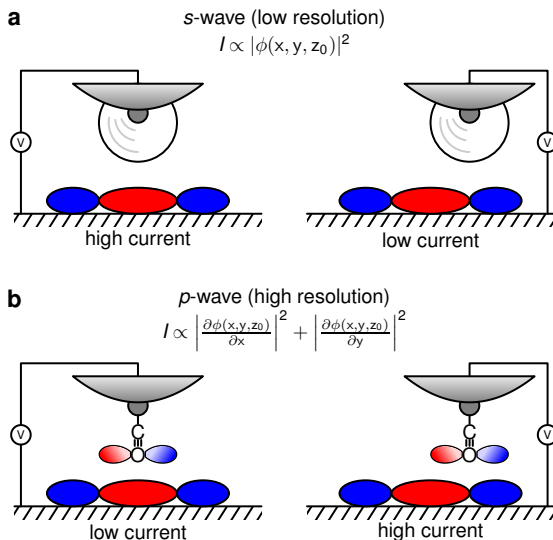


Fig. 1 Characteristics of different angular-momentum contributions. (a) Illustration of an *s*-wave contribution for the tip. In the MO region of high electron density, the tunneling current is high (left panel), while the tunneling current is low above the MO nodal region (right panel). (b) Illustration of a *p*-wave contribution for the tip. In the MO region of high electron density, the tunneling current is low (left panel), while the tunneling current is high above the MO nodal region (right panel).

STM simulation method, which was recently developed by us using the Bardeen’s approximation[16, 30], to build the dataset. For our approach, we opted for the U-Net model[23], which is well-suited for the segmentation task required to distinguish the spatially separable *s*- and *p*-wave signals. Previous investigations have shown that U-Net performs well on small datasets[31, 32], making it an ideal choice for our needs.

The architecture of STM-Net is illustrated in Fig. 2a (see Methods for more details). To demonstrate the advantage of U-Net on small datasets, we analyzed the learning curve of STM-Net (Fig. 2b). Strikingly, with a small training set, i.e., starting from just 10% of the dataset (corresponding to only 24 images), STM-Net was able to achieve satisfactory prediction results, with peak signal-to-noise ratio (PSNR) values above the threshold of 37 dB (see Methods for PSNR calculation details, as well as Supplementary Section 1 and Supplementary Fig. 1 for its relationship to the quality of the output images). With further increases in training set size, the PSNR of STM-Net eventually exceeded 43 dB (Fig. 2b), signifying that the outputs were highly consistent with the ground truth *s*-wave images. Similar convergence trends were observed for the other evaluation metrics (Extended Data Fig. 1).

We chose benzo[*m*]naphtho[2,3-*c*]tetrphene (BNT) as a representative molecule to illustrate the working procedure of STM-Net (Fig. 2c). The HOMO of the BNT molecule predominantly resides on two parallel triphenyl units, with a moderate distribution over the phenyl ring at the lower left corner. When imaging the HOMO of BNT using a CO-functionalized tip, two band-like patterns with four dark holes were observed (top-left panel in Fig. 2c), which were quite different from the calculated

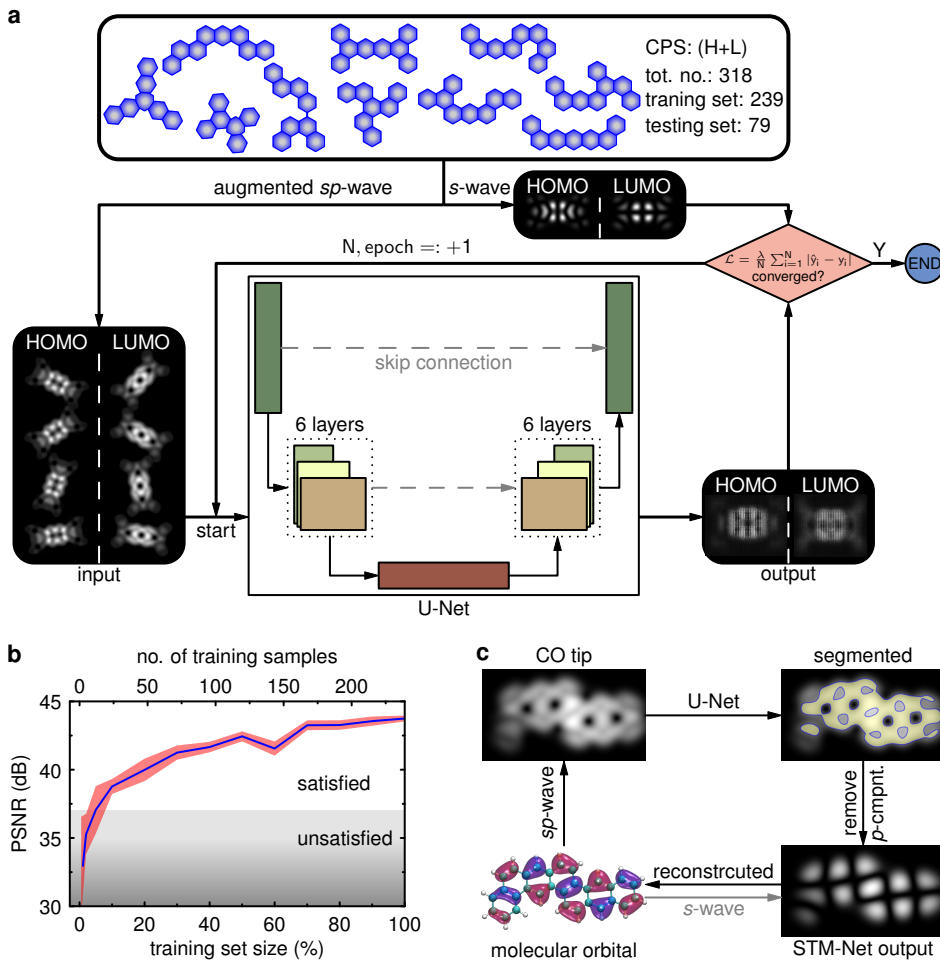


Fig. 2 STM-Net architecture and results. (a) Schematic of the training procedure for STM-Net (see details in Methods). (b) The learning curve for PSNR of STM-Net. The pink-shaded region represents the 95% confidence interval obtained from 10 separate training runs. The blue line shows the mean PSNR values averaged across these 10 training runs. The gray-shaded region indicates the performance region of unsatisfied models. (c) Example of MO reconstruction by STM-Net. Bottom-left: Calculated HOMO of BNT at the DFT level. Top-left: STM image obtained with the CO-functionalized tip, which emulates an *sp*-mix wave. Top-right: *p*-wave contributions identified by STM-Net (highlighted in yellow). Bottom-right: The output image generated by STM-Net.

MO as anticipated. Using STM-Net, the *p*-wave contributions were accurately isolated (yellow shadows of the top-right panel in Fig. 2c). By removing the unwanted *p*-wave signals, the output image from STM-Net (bottom-left panel in Fig. 2c) faithfully reproduces all the details of the corresponding MO. It should be stressed that acquiring a high-resolution *s*-wave image is inherently challenging in experiments as previously discussed. Thus, STM-Net introduces the first general machine learning framework capable of reconstructing pristine MOs from high-resolution STM images that contain undesired *p*-wave contributions. By leveraging the intrinsic connection between a

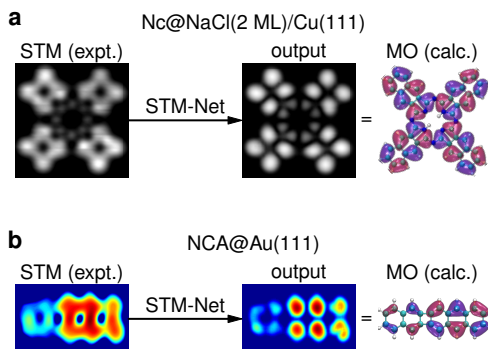


Fig. 3 Application of STM-Net to experimental images. (a) Experimentally measured STM image for the HOMO of naphthalocyanine (Nc) adsorbed on a NaCl(2 ML)/Cu(111) substrate under a CO-functionalized tip (left, reprinted with permission from ref. 14. Copyright 2011 by the American Physical Society). The output of the STM image after processing by STM-Net (middle) and the calculated HOMO at the DFT level. (b) Experimentally measured STM image for the HOMO of an NCA molecule adsorbed on the Au(111) surface with a CO-functionalized tip (left). The output of the STM image after processing by STM-Net (middle) and the calculated HOMO at the DFT level (right).

task in chemistry and an algorithm in machine learning, STM-Net achieves remarkable success that is unattainable for traditional image recognition or transformation algorithms (Supplementary Sections 2-3 and Supplementary Figs. 2-4).

Application of STM-Net to Experimental Images

The physics-driven nature of STM-Net ensures its strong generalization ability. To demonstrate this capability, we first applied STM-Net directly to the experimentally measured STM images for the HOMO of a naphthalocyanine (Nc) adsorbed on an insulating NaCl thin film covered Cu(111) surface using a CO-decorated tip^[14]. The NaCl film acted as a spacer, effectively decoupling the molecule from the Cu(111) substrate, which created a condition that closely resembled that in STM-Net. It is noteworthy that Nc contains nitrogen atoms and heterogeneous pentagonal rings, which significantly differ from the phenyl-based PAHs in the STM-Net dataset. Despite these differences, the STM-Net output based on the experimentally measured STM image accurately reproduces the MO characteristics of Nc (Fig. 3a). Specifically, STM-Net not only successfully removed the *p*-wave contributions from the bright lobe patterns but also effectively corrected the symmetry of the eight interior patterns (Extended Data Fig. 2). This success can be largely attributed to the high resolution of the original image, facilitated by the decoupling effect provided by the NaCl film.

Although decoupling the substrate’s perturbation on molecular electronic states can enhance the resolution, introducing a spacer requires extra experimental effort. In most STM experiments, the standard setup involves only inert metallic substrates. In this context, metallic substrates not only serve as supports for molecules but also provide adatoms to facilitate on-surface synthesis^[33]. Thus, reconstructing pristine MOs from STM images taken on metallic surfaces poses a more significant challenge for STM-Net. To address this issue, we examined the product of the debromination

cyclization and the subsequent dimerization reaction of 2,3-bis(dibromomethyl) naphthalene on an Au(111) substrate, yielding naphtho[2',3':3,4]cyclobuta[1,2-b]anthracene (NCA, Supplementary Section 4 and Supplementary Fig. 5)[34]. NCA features a four-membered ring, a structure not previously encountered in the STM-Net dataset. The STM image for the HOMO of NCA adsorbed on the Au(111) surface is inevitably affected by the metallic substrate, resulting in considerable distortions (left panel in Fig. 3b). Despite these challenges, STM-Net successfully mitigates much of the noise signals as well as the p -wave contributions (middle panel in Fig. 3b). As a result, the STM-Net output not only clearly delineates the critical node information but also accurately reflects the fact that the MO is concentrated on the anthracene moiety to the right of the four-membered ring (right panel in Fig. 3b).

The above cases not only validate the generalization capability of STM-Net but also highlight its ability to analyze molecular structures, offering a new means for identifying products in on-surface synthesis. Particularly, when nc-AFM fails to deliver conclusive structural information, high-resolution STM images obtained with functionalized tips combined with the analysis capabilities of STM-Net present a powerful alternative for structural analysis.

Adaptation of STM-Net to different tip states

The relative ratios of s - and p -wave contributions for a CO-decorated tips depend on the interaction between CO and the metallic tip[14, 17, 35]. The physics-driven nature of STM-Net enables its adaption to different tip states. As an extreme condition, we illustrate that the framework can be adapted for constructing MOs from images acquired using a pure p -wave tip. The network architecture is kept consistent, with the only modification being the input used for the training: specifically replacing sp -wave STM images with p -wave STM images (Extended Data Fig. 3). The PSNR learning curve exhibits almost identical average behavior compared to the previous setup, with a converged result exceeding 43 dB again, although the statistic region of individual learning processes is increased (Fig. 4a). This increased variation is also observed in the other two evaluation metrics, especially when the training size exceeds 30% (Extended Data Fig. 4). Such a heightened variation should be attributed to the extra step required for transforming p -wave characteristics into their s -wave equivalents.

To further illustrate the working procedure of STM-Net under these conditions, we again use the BNT molecule as an example (Fig. 4b). The STM image for the HOMO of BNT under a specially CO-decorated tip with pure p -wave state exhibits multiple holes. After training, STM-Net accurately identifies the regions with these holes that require padding for reconstructing the s -wave image (yellow circles in the top-right panel of Fig. 4b). By removing all p -wave signals and subsequently filling in the identified holes, STM-Net outputs the s -wave image (bottom-right panel in Fig. 4b), which precisely represents the MO distribution of BNT.

Conclusion

MO is a key concept in general chemistry, where directly observing MOs in real space is a fundamental pursuit of significant scientific importance. Although considerable

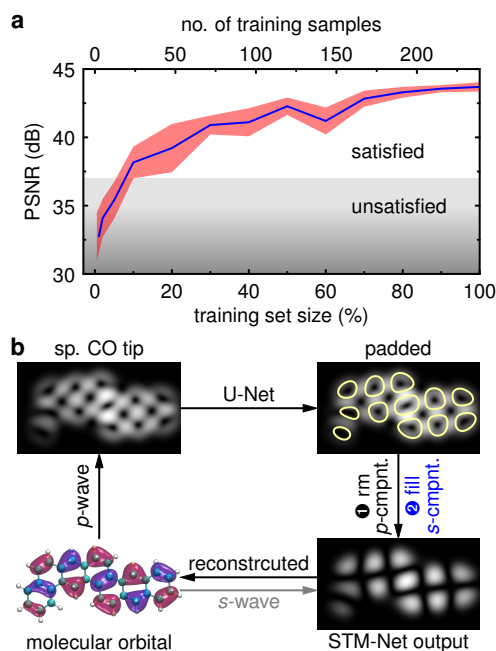


Fig. 4 Adaptation of STM-Net to p -to- s . (a) The learning curve for PSNR of the p -to- s STM-Net. The pink-shaded region represents the 95% confidence interval obtained from 10 separate training runs. The blue line shows the mean PSNR values averaged across these 10 training runs. The gray-shaded region indicates the performance region of unsatisfied models. (b) Example of MO reconstruction by the p -to- s STM-Net. Bottom-left: Calculated HOMO of BNT at the DFT level. Top-left: STM image obtained with a specially CO-functionalized tip in a pure p -state. Top-right: s -wave contributions identified by the p -to- s STM-Net (yellow circles). Bottom-right: The output image generated by the p -to- s STM-Net.

progress has been made with the aid of STM, it remains a substantial challenge, as STM images on the surfaces, acquired using functional tips, introduce unwanted components other than the intrinsic MOs of the molecules under study. We addressed this issue by developing a physics-driven AI network, named STM-Net. This network effectively eliminates the adverse effects of high-angular-momentum contributions from functionalized tips by accurately learning to separate the distinct features originating from the quantum interference, enabling the accurate reconstruction of frontier MOs. These findings highlight the principle of using physics-driven AI algorithms to solve chemical problems, providing a practical route for high-precision MO imaging. The proposed framework is expected to be extended to diverse types of decorated tips and more complicated molecular systems, establishing a research paradigm that closely integrates quantum chemistry theories with experimental characterization.

Methods

Architecture of STM-Net

The architecture of STM-Net is based on the U-Net model[23] with several modifications. For instance, strided convolution layers have been used in place of pooling layers; leaky ReLU activation functions were used in the down-sampling layers to prevent gradient vanishing; and transposed convolutions were employed instead of upsampling (interpolation) followed by a convolutional layer. The code of STM-Net has been made publicly available[36].

The specific U-Net encoder and decoder in STM-Net were structured as follows:

-U-net encoder: C₆₄-C₁₂₈-C₂₅₆-C₅₁₂-C₅₁₂-C₅₁₂-C₅₁₂

-U-Net Decoder: CD₅₁₂-CD₁₀₂₄-C₁₀₂₄-C₁₀₂₄-C₅₁₂-C₂₅₆-C₁₂₈

where C_{*i*} represents a convolution-batch normalization-ReLU layer with *i* filters and CD_{*j*} indicates a convolution-batch normalization-Dropout-ReLU layer with a 50% dropout rate (Supplementary Section 5 and Supplementary Figs. 6-7). All convolution layers utilized a 4 × 4 spatial filter with a stride of 2. This configuration implies that features were down-sampled and up-sampled by a factor of 2 in the encoder and decoder.

A convolution layer was attached to the final decoder layer to map the output to the required number of channels (1 in the present work), followed by a Tanh activation function as

$$\text{Tanh}(x) = \frac{e^x - e^{-x}}{e^x + e^{-x}}. \quad (1)$$

All ReLU activation functions in the encoder were replaced by leaky ReLU, defined as

$$\text{LeakyReLU}(x) = \max(0, x) + 0.2 \min(0, x). \quad (2)$$

In the decoder, the ReLU activation function

$$\text{ReLU}(x) = \max(0, x) \quad (3)$$

was used. The U-Net architecture includes skip connections that link the activation output of each encoder layer *i* to the corresponding decoder layer *n* - *i*, where *n* is the total number of layers. These skip connections double the number of channels in the decoder compared to the encoder. Batch normalization is not applied to the first C₆₄ layer in the encoder.

Training parameters of STM-Net

We first translated each STM image to focus on the central region and then resized the image to 286 × 286 pixels. Subsequently, random cropping was applied to further adjust the images to a final size of 256 × 256 pixels. This approach prevents the model from over-relying on the fixed positions of objects in the images. The process of jittering with some further random mirroring also enhances the model’s robustness against minor variations, improving its generalization capability. All networks were trained

from scratch, with weights initialized from a Gaussian distribution with a mean of 0 and a standard deviation of 0.02.

The dataset consisted of 318 theoretically simulated STM images generated at the density functional theory (DFT) level (section ‘‘Dataset in STM-Net’’ in Methods) and was trained over 1000 epochs with a batch size of 16. The dataset was randomly divided into training and testing sets in a 75:25 ratio (Supplementary Figs. 8-15). During the first 500 epochs, the learning rate was set to 0.0002, and for the remaining 500 epochs, it linearly decayed to 0. The training process utilized the loss function as:

$$\mathcal{L}_1 = \frac{1}{N \cdot C \cdot H \cdot W} \sum_{n=1}^N \sum_{c=1}^C \sum_{h=1}^H \sum_{w=1}^W |I_{n,c}^{\text{out}}(h, w) - I_{n,c}^{\text{gt}}(h, w)|, \quad (4)$$

where N is the batch size, C is the number of image channels, H (W) is the height (width) of the images, I^{out} is the output image of STM-Net, and I^{gt} is the ground truth of the s -wave STM image. In this work, we set $N = 16$, $C = 1$, $H = 256$, and $W = 256$. The Adam optimizer with $\beta_1 = 0.5$ and $\beta_2 = 0.999$ was used for back-prorogation, To process the real experimental measurements using STM-Net, the dataset was augmented by rotating each image in every 5° increment as illustrated in Fig. 2a and Extended Data Fig. 3. This augmentation expands the dataset by a factor of 72.

Dataset in STM-Net

We selected 159 representative hexagonal PAHs from the COMPAS project[29] database (Supplementary Section 6). The molecular structures were first optimized in the gas phase using DFT at the X3LYP[37] level with the cc-pVTZ basis set[38–41], as implemented in the Gaussian 16 suite of programs[42]. This setting corresponds to isolated molecular systems on insulating substrates in STM measurements. After obtaining the wavefunctions of the isolated molecules, the HOMO and LUMO STM images were simulated using Bardeen’s approximation[16, 30]. Specifically, the tunneling current in atomic units is given by

$$I = 2\pi \int_{-\infty}^{\infty} [f_t(E - eV) - f_s(E)] \rho_t(E - eV) \rho_s(E) |M_{st}|^2 dE, \quad (5)$$

where subscripts ‘‘ t ’’ and ‘‘ s ’’ refer to functions associated with the tip and substrate, f stands for the Fermi-Dirac distribution, e is the elementary charge, V is the applied bias voltage, ρ is the density of states, and M_{st} is the transfer Hamiltonian matrix element. The energy reference levels for the tip and substrate are set to the corresponding Fermi levels (E_F) under the applied bias. High-resolution STM measurements were typically performed at low temperatures. For isolated molecules, ρ_s becomes a Dirac δ -function, representing discrete states. In this scenario, the tunneling current can be simplified as

$$I = 2\pi \sum_{E_s=E_F}^{E_F+eV} \rho_t(E_s - eV) |M_{st}|^2 \quad (6)$$

where E_s denotes the molecular energy levels. In a practical STM image simulation, ρ_t was assumed to be a constant.

The transfer Hamiltonian matrix can be calculated as[16, 30]

$$M_{st} = -\frac{1}{2} \int_{\Sigma} (\Psi_t^* \nabla \Psi_s - \Psi_s^* \nabla \Psi_t) \cdot ds \quad (7)$$

Here, Ψ_t and Ψ_s denote the quasi-particle wavefunctions of the tip and sample, respectively, Σ represents the separation surface between the tip and sample regions, and ds is the surface element vector on Σ . In our calculations, s - and p -type Gaussian functions with an exponent of $\alpha = 0.25 \text{ Bohr}^{-2}$ were used to mimic the s - and p -wave tips, respectively. For the sp -mixed tip, the contributions of s - and p -wave were set to 1:1 and z_0 was set to 0.1 \AA above the molecules to mimic the behavior of a typical CO-functionalized STM tip[14, 16, 17].

Evaluation metrics for STM-Net

We evaluated the outputs of STM-Net using widely-recognized metrics, namely PSNR, structural similarity index measure (SSIM), and learned perceptual image patch similarity (LPIPS). Given that these metrics exhibited generally consistent trends, PSNR, which is straightforward and widely applicable, was chosen in the main text.

PSNR[43] measures the ratio between the maximum possible value of a signal and the degradation caused by a noise, providing an objective quantification of image restoration degree by assessing the mean squared error (MSE). The definition of PSNR is

$$\text{PSNR} = 20 \log_{10} \left(\frac{\text{MAX}_f}{\sqrt{\text{MSE}}} \right), \quad (8)$$

where MAX_f represents the maximum possible pixel value of the image, and MSE can be calculated as

$$\text{MSE} = \frac{1}{H \cdot W} \sum_{h=1}^H \sum_{w=1}^W \|I^{\text{out}}(h, w) - I^{\text{gt}}(h, w)\|^2. \quad (9)$$

The logarithmic decibel scale used in PSNR calculation is particularly suitable for evaluating signals that have a broad dynamic range.

SSIM[44] evaluates image quality from a perceptual perspective, considering degradation in structural information and incorporating the effects of luminance and contrast masking. Unlike PSNR, which focuses on pixel-wise differences, SSIM emphasizes changes in structural information and calculates a composite similarity score that reflects these aspects along with luminance and contrast (see details in Supplementary Section 7.1).

LPIPS[45] uses deep learning techniques to evaluate visual perceptual similarity. Through pre-trained convolutional neural networks, it extracts high-level features from images to calculate perceptual similarity score. This metrics especially suitable for tasks like generative model evaluation or those requiring high perceptual accuracy (see details in Supplementary Section 7.2).

Experimental STM measurements

The STM images of NCA were obtained at 4.6 K with a commercial LT-STM (Scienta Omicron). The single crystal Au(111) was supplied by MaTeck GmbH and was cleaned through cyclic Ar-ion sputtering and annealing. The precursors (2,3-bis(dibromomethyl)naphthalene)[34] were deposited onto the Au(111) surfaces held at room-temperature by organic molecular beam deposition technique from a commercial evaporator (Kentax GmbH). The sample of NCA was prepared by on-surface reactions of the precursors (thermal annealing at 400 K for 30 min). To minimize the interference of the Au(111) substrate, the dI/dV mapping of NCA was conducted in the constant-height mode by using a CO-functionalized tip with a resonance frequency of $f_0 \approx 27.5$ kHz and a quality factor $Q > 10^4$. All STM images were observed under ultra-high vacuum conditions with a base pressure better than 1.0×10^{-10} mbar.

References

- [1] Mulliken, R. S. Electronic structures of polyatomic molecules and valence. II. General considerations. *Phys. Rev.* **41**, 49 (1932).
- [2] Fukui, K., Yonezawa, T. & Shingu, H. A molecular orbital theory of reactivity in aromatic hydrocarbons. *J. Chem. Phys.* **20**, 722–725 (1952).
- [3] Woodward, R. B. & Roald, H. Stereochemistry of electrocyclic reactions. *J. Am. Chem. Soc.* **87**, 395–397 (1965).
- [4] Mulder, P. Are orbitals observable? *Int. J. Philos. Chem.* **17**, 24–35 (2011).
- [5] Pham, B. Q. & Gordon, M. S. Can orbitals really be observed in scanning tunneling microscopy experiments? *J. Phys. Chem. A* **121**, 4851–4852 (2017).
- [6] Zuo, J.-M., Kim, M., O’keeffe, M. & Spence, J. Direct observation of d -orbital holes and Cu–Cu bonding in Cu_2O . *Nature* **401**, 49–52 (1999).
- [7] Repp, J., Meyer, G., Stojković, S. M., Gourdon, A. & Joachim, C. Molecules on insulating films: Scanning-tunneling microscopy imaging of individual molecular orbitals. *Phys. Rev. Lett.* **94**, 026803 (2005).
- [8] Gross, L. Recent advances in submolecular resolution with scanning probe microscopy. *Nat. Chem.* **3**, 273–278 (2011).
- [9] Kitou, S. *et al.* Successive dimensional transition in $(\text{TMTTF})_2\text{PF}_6$ revealed by synchrotron X-ray diffraction. *Phys. Rev. Lett.* **119**, 065701 (2017).
- [10] Tersoff, J. & Hamann, D. R. Theory of the scanning tunneling microscope. *Phys. Rev. B* **31**, 805 (1985).
- [11] Chen, C. J. *Introduction to Scanning Tunneling Microscopy* 3 edn (Oxford University Press, USA, 2021).

- [12] Duan, S. *et al.* Theoretical modeling of plasmon-enhanced raman images of a single molecule with subnanometer resolution. *J. Am. Chem. Soc.* **137**, 9515–9518 (2015).
- [13] Duan, S., Zhang, I. Y., Xie, Z. & Xu, X. Identification of water hexamer on cu(111) surfaces. *J. Am. Chem. Soc.* **142**, 6902–6906 (2020).
- [14] Gross, L. *et al.* High-resolution molecular orbital imaging using a *p*-wave STM tip. *Phys. Rev. Lett.* **107**, 086101 (2011).
- [15] Chen, C. J. Tunneling matrix elements in three-dimensional space: The derivative rule and the sum rule. *Phys. Rev. B* **42**, 8841 (1990).
- [16] Duan, S., Tian, G. & Xu, X. A general framework of scanning tunneling microscopy based on Bardeen’s approximation for isolated molecules. *JACS Au* **3**, 86–92 (2022).
- [17] Duan, S. & Xu, X. Accurate simulations of scanning tunneling microscope: Both tip and substrate states matter. *J. Phys. Chem. Lett.* **14**, 6726–6735 (2023).
- [18] Beyan, E. V. P., Rossy, A. G. C. *et al.* A review of AI image generator: influences, challenges, and future prospects for architectural field. *J. Artif. Intell. Archt.* **2**, 53–65 (2023).
- [19] Castiglioni, I. *et al.* AI applications to medical images: From machine learning to deep learning. *Phys. Medica* **83**, 9–24 (2021).
- [20] Krizhevsky, A., Sutskever, I. & Hinton, G. E. *ImageNet classification with deep convolutional neural networks.* (eds Pereira, F., Burges, C. J., Bottou, L. & Weinberger, K. Q.) *Advances in Neural Information Processing Systems*, Vol. 25 (Curran Associates, Inc., 2012).
- [21] Yang, H. *et al.* MatterSim: A deep learning atomistic model across elements, temperatures and pressures. *arXiv preprint arXiv:2405.04967* (2024).
- [22] Alberts, I. L. *et al.* Large language models (LLM) and ChatGPT: What will the impact on nuclear medicine be? *Eur. J. Nucl. Med. Mol. Imaging* **50**, 1549–1552 (2023).
- [23] Ronneberger, O., Fischer, P. & Brox, T. *U-Net: Convolutional networks for biomedical image segmentation.* (eds Navab, N., Hornegger, J., Wells, W. M. & Frangi, A. F.) *Medical Image Computing and Computer-Assisted Intervention – MICCAI*, 234–241 (Springer International Publishing, Cham, 2015).
- [24] Goodfellow, I. *et al.* Generative adversarial networks. *Commun. ACM* **63**, 139–144 (2020).

- [25] Ho, J., Jain, A. & Abbeel, P. Denoising diffusion probabilistic models. *Adv. Neural Inf. Process. Syst.* **33**, 6840–6851 (2020).
- [26] Krull, A., Hirsch, P., Rother, C., Schiffrin, A. & Krull, C. Artificial-intelligence-driven scanning probe microscopy. *Commun. Phys.* **3**, 54 (2020).
- [27] Su, J. *et al.* Intelligent synthesis of magnetic nanographenes via chemist-intuited atomic robotic probe. *Nat. Synth.* **3**, 466–476 (2024).
- [28] Zhu, Z. *et al.* Autonomous scanning tunneling microscopy imaging via deep learning. *J. Am. Chem. Soc.* **146**, 29199–29206 (2024).
- [29] Wahab, A., Pfuderer, L., Paenurk, E. & Gershoni-Poranne, R. The COMPAS project: A computational database of polycyclic aromatic systems. Phase 1: *cata*-Condensed polybenzenoid hydrocarbons. *J. Chem. Inf. Model.* **62**, 3704–3713 (2022).
- [30] Bardeen, J. Tunnelling from a many-particle point of view. *Phys. Rev. Lett.* **6**, 57–59 (1961).
- [31] Liu, F. & Wang, L. UNet-based model for crack detection integrating visual explanations. *Constr. Build. Mater.* **322**, 126265 (2022).
- [32] Prasad, P. J. R., Elle, O. J., Lindseth, F., Albrechtsen, F. & Kumar, R. P. *Modifying U-Net for small dataset: A simplified U-Net version for liver parenchyma segmentation.* (eds Mazurowski, M. A. & Drukker, K.) *Medical Imaging 2021: Computer-Aided Diagnosis*, Vol. 11597, 115971O. International Society for Optics and Photonics (SPIE, 2021).
- [33] Li, S. *et al.* Structural phase transitions of molecular self-assembly driven by nonbonded metal adatoms. *ACS Nano* **14**, 6331–6338 (2020).
- [34] Tang, Y. *et al.* On-surface debromination of 2,3-bis(dibromomethyl)- and 2,3-bis(bromomethyl) naphthalene: Dimerization or polymerization? *Angew. Chem. Int. Ed.* **61**, e202204123 (2022).
- [35] Mohn, F., Gross, L., Moll, N. & Meyer, G. Imaging the charge distribution within a single molecule. *Nat. Nanotechnol.* **7**, 227–231 (2012).
- [36] STM-Net: A physics-driven deep learning framework for constructing molecular orbitals from STM images. https://github.com/ZeHeru/STM_net.
- [37] Xu, X. & Goddard III, W. A. The X3LYP extended density functional for accurate descriptions of nonbond interactions, spin states, and thermochemical properties. *Proc. Natl. Acad. Sci. USA* **101**, 2673–2677 (2004).
- [38] Dunning Jr, T. H. Gaussian basis sets for use in correlated molecular calculations. I. The atoms boron through neon and hydrogen. *J. Chem. Phys.* **90**, 1007–1023

- (1989).
- [39] Peterson, K. A., Woon, D. E. & Dunning Jr, T. H. Benchmark calculations with correlated molecular wave functions. IV. The classical barrier height of the $\text{H}+\text{H}_2\rightarrow\text{H}_2+\text{H}$ reaction. *J. Chem. Phys.* **100**, 7410–7415 (1994).
 - [40] Woon, D. E. & Dunning Jr, T. H. Gaussian basis sets for use in correlated molecular calculations. III. The atoms aluminum through argon. *J. Chem. Phys.* **98**, 1358–1371 (1993).
 - [41] Kendall, R. A., Dunning Jr, T. H. & Harrison, R. J. Electron affinities of the first-row atoms revisited. Systematic basis sets and wave functions. *J. Chem. Phys.* **96**, 6796–6806 (1992).
 - [42] Frisch, M. J. *et al.* Gaussian 16 Revision C.01 (2016). Gaussian Inc. Wallingford CT.
 - [43] Korhonen, J. & You, J. Burnett, I. (ed.) *Peak signal-to-noise ratio revisited: Is simple beautiful?* (ed. Burnett, I.) *Fourth International Workshop on Quality of Multimedia Experience*, 37–38 (2012).
 - [44] Wang, Z., Bovik, A. C., Sheikh, H. R. & Simoncelli, E. P. Image quality assessment: from error visibility to structural similarity. *IEEE Trans. Image Process.* **13**, 600–612 (2004).
 - [45] Zhang, R., Isola, P., Efros, A. A., Shechtman, E. & Wang, O. *The unreasonable effectiveness of deep features as a perceptual metric.* (eds Forsyth, D., Laptev, I., Oliva, A. & Ramanan, D.) *IEEE/CVF Conference on Computer Vision and Pattern Recognition (CVPR)*, 586–595 (2018).

Acknowledgements

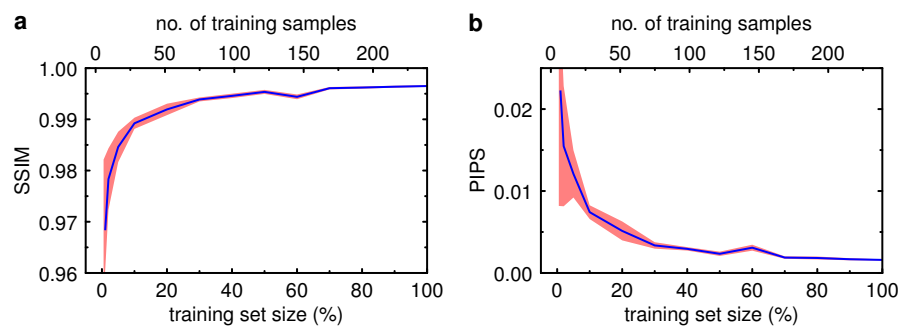
This work was supported by the National Key R&D Program of China (2024YFA1208104), the National Natural Science Foundation of China (Nos. 22393911, 22473028, U24A20496, and 22472114), and the Innovation Program for Quantum Science and Technology (Nos. 2021ZD0303301 and 2021ZD0303305).

Author contributions

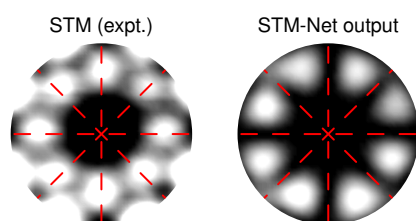
X.X. and S.D. conceived the research. X.X., S.D., H.Z. and L.C. jointly supervised the work. Y.Z. performed the simulations. R.X. performed the experiments. X.X., S.D., H.Z., Y.Z. and R.X. interpreted the data. All authors contributed to the writing of the manuscript.

Competing interests

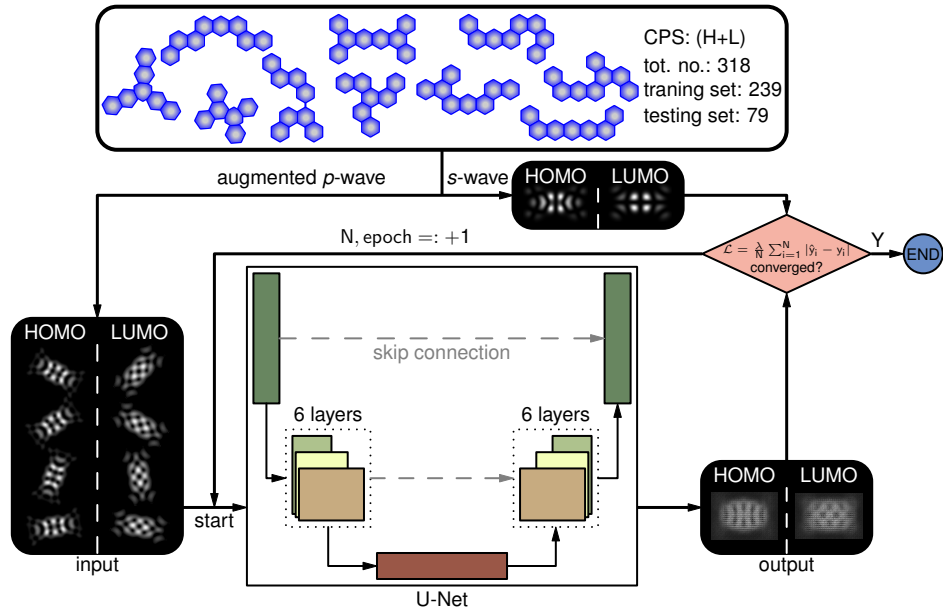
The authors declare no competing interests.



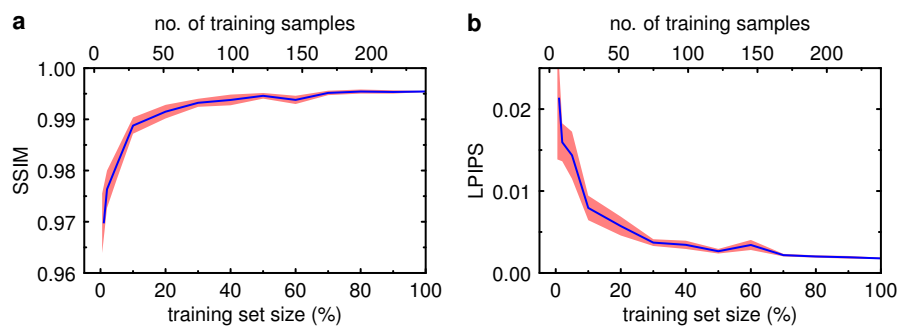
Extended Data Fig. 1 Other metrics for STM-Net. The learning curves for SSIM (a) and LPIPS (b) of STM-Net. The pink-shaded region represents the 95% confidence interval obtained from 10 separate training runs. The blue line shows the mean metrics values averaged across these 10 training runs.



Extended Data Fig. 2 Zoomed and rescaled Nc images. Zoomed and rescaled version of the experimentally measured STM image for the HOMO of Nc@NaCl(2 ML)@Cu(111) (left) and its corresponding STM-Net output (right). The red dashed lines indicate the nodal planes owing to the a_1 irreducible representation of the HOMO.



Extended Data Fig. 3 STM-Net architecture for a pure *p*-wave tip. Schematic of the STM-Net training process for the transformation of STM images under a pure *p*-wave tip to the corresponding images under an *s*-wave tip (see details in Methods).



Extended Data Fig. 4 Other evaluation metrics for the p -to- s STM-Net. The learning curves for SSIM (a) and LPIPS (b) of the p -to- s STM-Net. The pink-shaded region represents the 95% confidence interval obtained from 10 separate training runs. The blue line shows the mean metrics values averaged across these 10 training runs.